From Sugar to Flowers: A Transition of Shallow Cumulus Organization During ATOMIC

Pornampai Narenpitak[1,2], Jan Kazil[1,2], Takanobu Yamaguchi[1,2], Patricia Quinn[3], Graham Feingold[2]

[1]Cooperative Institute for Research in Environmental Sciences, University of Colorado Boulder, Boulder, Colorado, USA

[2]National Oceanic and Atmospheric Administration, Chemical Sciences Laboratory, Boulder, Colorado, USA

[3]National Oceanic and Atmospheric Administration, Pacific Marine Environmental Laboratory, Seattle, Washington, USA

Key Points:

- Lagrangian LES can reproduce the transition of shallow cumulus organization from sugar to flowers observed on Feb 2-3, 2020 during ATOMIC
- While large-scale upward vertical wind deepens the cloud layer, mesoscale wind renders moist areas moister assisting cloud organization
- Stronger large-scale upward motion strengthens the mesoscale circulation and accelerates the sugar-to-flowers transition process

Corresponding author: Pornampai Narenpitak, `pornampai.narenpitak@noaa.gov`

Abstract

The Atlantic Tradewind Ocean-Atmosphere Mesoscale Interaction Campaign (ATOMIC) took place in January–February 2020. It was designed to understand the relationship between shallow convection and the large-scale environment in the trade-wind regime. Lagrangian large eddy simulations, following the trajectory of a boundary-layer airmass, can reproduce a transition of trade cumulus organization from "sugar" to "flower" clouds with cold pools, observed on February 2–3. The simulations were driven with reanalysis large-scale meteorology and ATOMIC in-situ aerosol data. During the transition, large-scale upward motion deepens the cloud layer. The total water path and optical depth increase, especially in the moist regions where flowers aggregate. Mesoscale circulation leads to a net convergence of total water in the already moist and cloudy regions, strengthening the organization. Stronger large-scale upward motion reinforces the mesoscale circulation and accelerates the organization process by strengthening the cloud-layer mesoscale buoyant turbulence kinetic energy production.

Plain Language Summary

Fair-weather shallow clouds have different sizes and cloud properties. A field study called ATOMIC and EUREC^{4}A was designed to further understand the properties of these clouds. On February 2–3, very small and shallow "sugar" clouds grow into wider and deeper "flower" cloud clusters, no more than 3 km high. The clear spaces between the clouds expand. This study finds that local air circulation is responsible for making the moist and cloudy areas moister, and dry and cloud-free areas drier, enabling a process responsible for this transition. The large-scale vertical winds modulate the rate and strength of this process which occurs locally at smaller scales.

1 Introduction

Shallow clouds in a warm boundary layer continue to be a leading source of uncertainty in global climate models (i.e. Bony & Dufresne, 2005; Boucher et al., 2013; Zelinka et al., 2016). Previous studies have used high-resolution simulations and satellite imagery to understand the relationships between shallow cumulus properties and the large-scale atmospheric and oceanic conditions. For example, the Barbados Oceanographic and Meteorological Experiment (BOMEX) examined the turbulent dynamics of shallow cumuli using different large eddy simulation (LES) models (Siebesma et al., 2003). The Cloud

Feedback Model Intercomparison Project—Global Atmospheric System Study Intercomparison of Large Eddy Models and Single Column Models (CGILS) investigated the mechanisms of cloud feedback of shallow cumulus and stratocumulus under idealized climate change perturbations based on summertime subtropical atmospheric conditions in the Pacific Ocean (Zhang et al., 2013; Bretherton et al., 2013; Blossey et al., 2013). Bretherton and Blossey (2017) further explored a mechanism of shallow cumulus organization in different large-scale conditions, including those from BOMEX and one of the CGILS cases. Other studies have used LES models to explore the relationship between turbulent flux and cloud amount (Narenpitak & Bretherton, 2019), and processes associated with arc-shaped organization of shallow cumuli known as cold pools (i.e. Zuidema et al., 2017, and references therein). In addition, Mieslinger et al. (2019) examined how different meteorological conditions affect cloud properties across different oceanic basins using high resolution satellite imagery. The use of high resolution simulations and remote sensing tools over the years have enabled studies that lead to better understanding of shallow cumulus processes.

A field campaign designed to study shallow convection in the trade wind region occurred in January–February, 2020 in the Atlantic Ocean east of Barbados. The Atlantic Tradewind Ocean–Atmosphere Mesoscale Interaction Campaign (ATOMIC) and its European counterpart, the European field campaign called Elucidating the Role of Clouds-Circulation Coupling in Climate (EUREC^{4}A), formed a field campaign that used instruments on research aircrafts and ships to observe the properties of shallow cumulus clouds in order to better understand their relationship with the large-scale environment (Quinn et al., 2020; Pincus et al., 2021; Stevens et al., 2021). Recent studies (i.e. Stevens et al., 2020; Rasp et al., 2020; Bony et al., 2020) have categorized the mesoscale organization of shallow cumuli based on the Moderate Resolution Imaging Spectroradiometer (MODIS) imagery into four types: sugar, gravel, fish, and flowers. Different states of organization have different cloud properties including boundary layer depth, amount of precipitation, cloud fraction, and cloud radiative effect.

On February 2–3, 2020, a transition from small and shallow clouds called “sugar” to larger and deeper clouds called “flowers” occurred over the field campaign region (Fig. 1a; animation in Movie S1 in the the Supporting Information (SI)). Backward trajectories following the airmass at 500 m altitude show that these flower clouds originated from a shallow sugar cloud layer northeast of the NOAA Research Vessel Ronald H. Brown

(RHB). Larger flowers with cold pools were observed to the southwest, closer to Barbados. This study uses a Lagrangian LES, with the domain following a boundary-layer trajectory (red box and yellow dots in Fig. 1a), to simulate this organization event. To understand the relationship between the large-scale vertical velocity and the transition of the mesoscale organization, an additional LES with modified large-scale vertical velocity is included.

The structure of this paper is as follows. Section 2 describes the simulation configurations and the observations used to initialize the simulations. Sections 3 shows the transition from sugar to flowers represented by the LES. Section 4 discusses the mechanisms that are important for the organization. Section 5 identifies the role of large-scale vertical motion on the sugar-to-flowers transition and the circulation at the mesoscale. Finally, conclusions are given in Section 6. Figures S1-S11 and Movies S1-S3 are found in the SI.

2 Data and Simulations

The System for Atmospheric Modeling (SAM) (Khairoutdinov & Randall, 2003) is employed. The large-scale environment (soundings) and forcings of the simulations are derived from the European Centre for Medium-Range Weather Forecasts (ECMWF) Reanalysis 5^{th} Generation (ERA5) (Hersbach et al., 2020), following the airmass at 500 m altitude through the location of the RHB (54.5°W and 13.9°N) at 17 UTC on February 2. The airmass trajectory was calculated by the Hybrid Single-Particle Lagrangian Integrated Trajectory (HYSPLIT) model (Stein et al., 2015; Rolph et al., 2017) in the ERA5 reanalysis. Since the trajectory moves approximately with the boundary layer, large-scale horizontal advection of the temperature and humidity is not included. Instead, to account for horizontal advection in the free troposphere, the temperature and humidity profiles of the simulation are nudged to the ERA5 soundings above the inversion with a 30 min relaxation time scale.

The control simulation (CTL) is configured with 100 m horizontal grid spacing and a horizontal domain extent of 192×192 km^2. The vertical grid spacing is 50 m, increasing geometrically from 5 km to the domain top at 8 km (total of 120 levels). Above that, the atmospheric profiles from ERA5 are used up to the top of atmosphere for the radiation calculation. The simulation uses a bulk two-moment (bin-emulating) microphysics

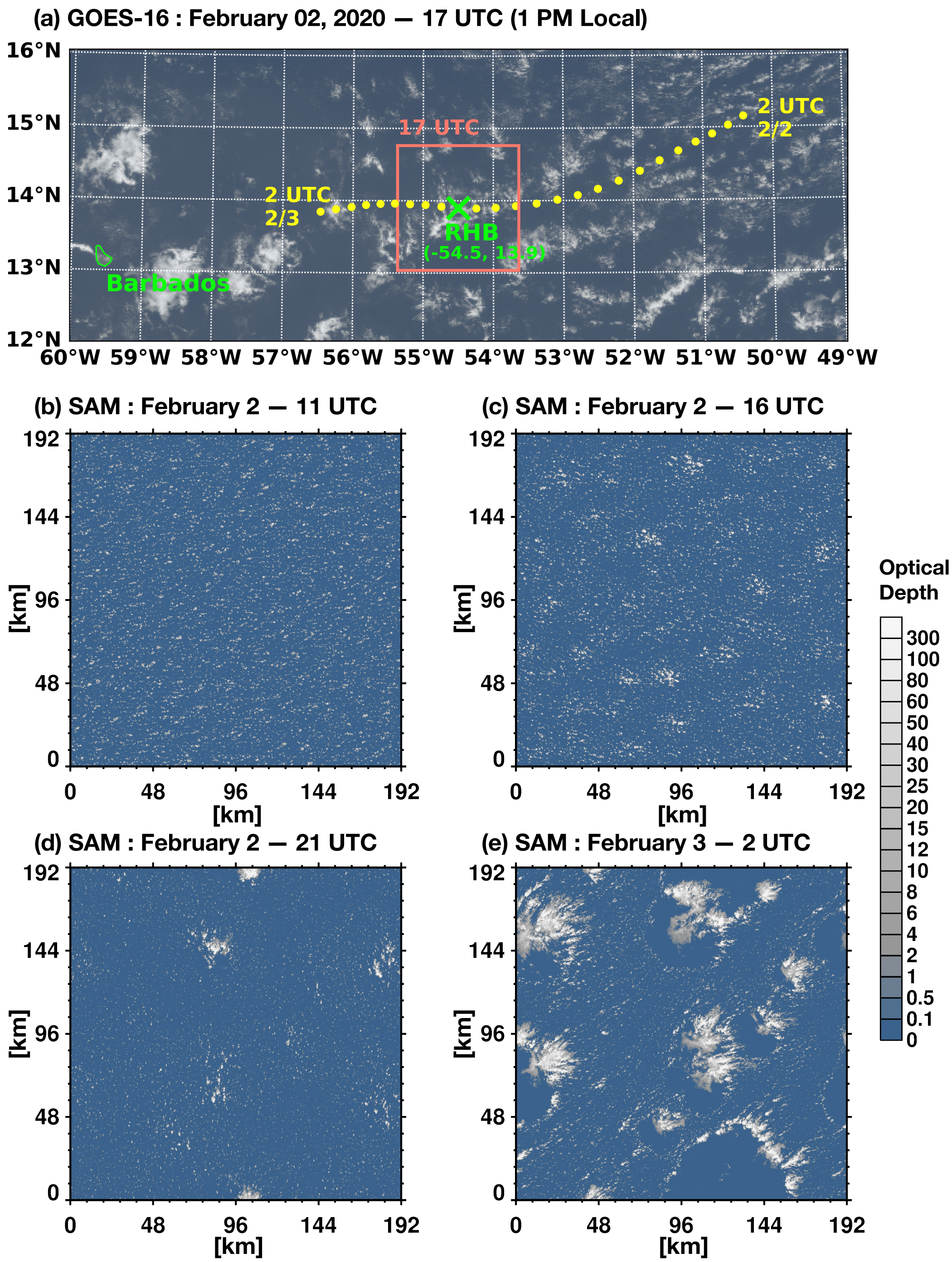

Figure 1. (a) A satellite image from the Geostationary Operational Environmental Satellite-16 (GOES-16) on February 2. The yellow dots represent hourly coordinates of the airmass-following trajectory on which the Lagrangian simulations are based. The red box indicates the simulation's 192×192 km^2 domain extent, centered at the Ronald H. Brown research ship (green '×') at 17 UTC. (b-d) Snapshots of total (cloud+rain) optical depth from the control simulation (CTL) shown at the designated times.

scheme (Feingold et al., 1998) and the Rapid Radiative Transfer Model for global climate model applications (RRTMG) radiation scheme (Mlawer et al., 1997) with time varying atmospheric profiles above the domain top and the diurnal cycle of solar radiation. The radiation is computed every 10 seconds. The model's time step is 2 seconds, and the duration of the simulation is 24 hours, from 2 UTC on February 2 to 2 UTC on February 3, 2020.

An additional simulation called WeakW is performed using the same model configuration as CTL, except with a modified vertical velocity (W) in the forcings. The W profiles for WeakW are 50% weaker than CTL during a period with strong upward motion, between 11 UTC and 19 UTC. Since SAM linearly extrapolates the hourly W forcing profiles to the model's time step, W in WeakW starts to diverge from CTL at 10 UTC, and converges again at 20 UTC (Fig. S1a-b).

There are two types of aerosol in the simulations: sea salt and mineral dust (Fig. S1c-f). They are initialized based on the in-situ measurements and are advected within the domain. The sea-salt particles interact with the cloud microphysics scheme, but not with radiation. The mineral dust is included and only coupled with the radiation but not with the microphysics, as it remains in the free troposphere. This is consistent with the observation, that mineral dust was present above the cloud layer east of Barbados between January 31 and February 3. See Section 1 of the SI for details on the initialization of the aerosol.

3 Transition of Shallow Cumuli: From Sugar to Flowers

Simulation CTL is able to reproduce the transition from sugar to flowers on February 2–3, 2020. Figure 1b-e and Movie S2 show the cloud state evolution. The sugar-to-flowers transition occurs between 8 UTC and 18 UTC. During this time, the sugar cloud field forms clusters, which then develop into contiguous aggregates and expand laterally to mature into flowers. Cumulus clouds interspersed between the flowers are suppressed compared to the initial sugar cloud field. After 20 UTC, the aggregated flowers produce precipitation, which partially evaporates before reaching the surface, resulting in cold downdrafts that produce cold pools adjacent to the flowers. A 3D snapshot of the cloud field at 2 UTC on February 3 (final time step) is shown in Figure S4.

3.1 Multiscale Partitioning

Although the simulations are run at 100 m grid spacing, it is helpful to coarse-grain the outputs into larger tiles. This approach partitions the results into contributions from the large-scale, mesoscale, and cumulus-scale processes. Coarse-graining filters out the details at the smaller scales that may be associated with shallow convection but are not relevant to the organization. This method was first introduced by Bretherton and Blossey (2017). The tile size of 16×16 km^2 is chosen for this study as it represents the horizontal variability of flower shallow cumuli in the simulations. See Section 2 of the SI for details on how the tile size is determined.

The partitioning of total water mixing ratio (q_t) is given by:

$$q_t = \overline{q_t} + q_t'' + q_t''' \quad . \tag{1}$$

The overline is the domain-mean, the double prime is the perturbation coarse-grained to 16×16 km^2 tiles, representing variability associated with the mesoscale (≥16 km). The triple prime represents variability associated with cumulus-scale processes (<16 km). The partitioning is detailed in Section 3 of the SI.

The coarse-grained outputs are sorted by total water path (TWP, a sum of vertically integrated water vapor, cloud, and rain) and binned into quartiles. Quartile 1 (Q1) represents the driest and cloud-free areas while Quartile 4 (Q4) represents the moistest and cloudiest areas of the simulation. The 16×16 km^2 tiles in each quartile are not necessarily adjacent to one another.

3.2 Shallow Convection Organization

Figure 2 shows the evolution of the simulations. The thick solid lines represent the results from CTL. Sea surface temperature (SST) increases as the trajectory moves southwestward, and remains constant as the trajectory moves westward. The deepening of the cloud layer in CTL occurs after 6 UTC and becomes more obvious after 10 UTC, when the domain-mean vertical velocity ($\overline{w}$) shifts from negative to positive, helping the cloud layer to deepen (Fig 2b). After 20 UTC, the cloud depth remains constant as the boundary layer encounters large-scale subsidence.

The domain-mean TWP increases as the cloud layer deepens during the transition process (Fig. 2d). As the organization strengthens, the TWP distribution becomes more

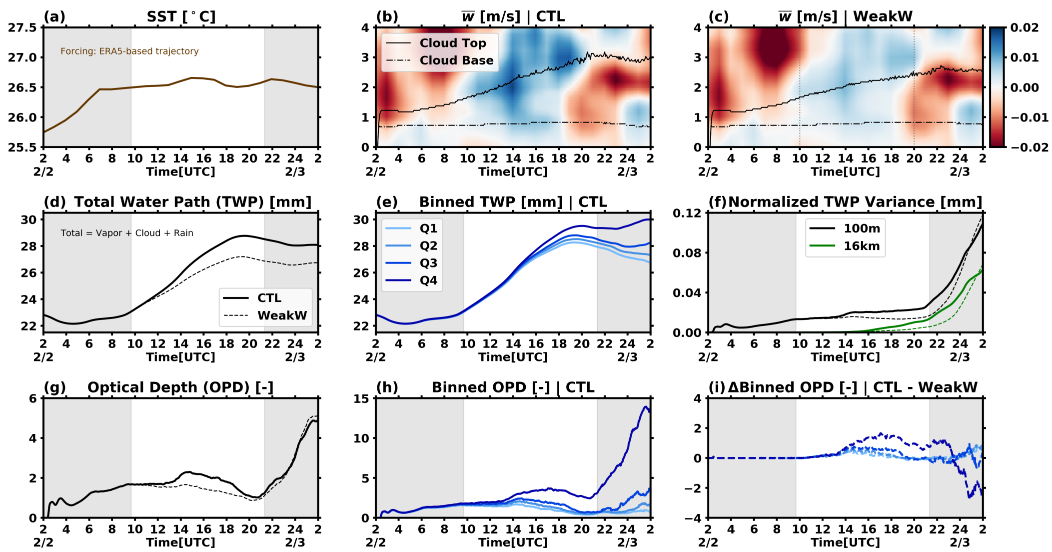

Figure 2. Time series of: (a) domain-mean sea surface temperature; (b) domain-mean vertical velocity, and cloud top and base heights, from CTL; (c) as in Panel (b) but for the weaker vertical velocity simulation (WeakW); (d) domain-mean total water path (TWP) of both CTL (solid) and WeakW (dash); (e) TWP sorted into quartiles from CTL; (f) variances of TWP computed at the full resolution (black) and the 16 km coarse-grained resolution (green), from both CTL (solid) and WeakW (dash); (g) domain-mean optical depth (OPD) from both simulations; (h) OPD, binned by TWP, from CTL; (i) the change in OPD, binned by TWP, between CTL and WeakW. Grey shading is applied between the daylight hours of 5:48 am and 17:23 pm (local time), when the top-of-atmosphere incoming shortwave radiation exceeds zero in SAM.

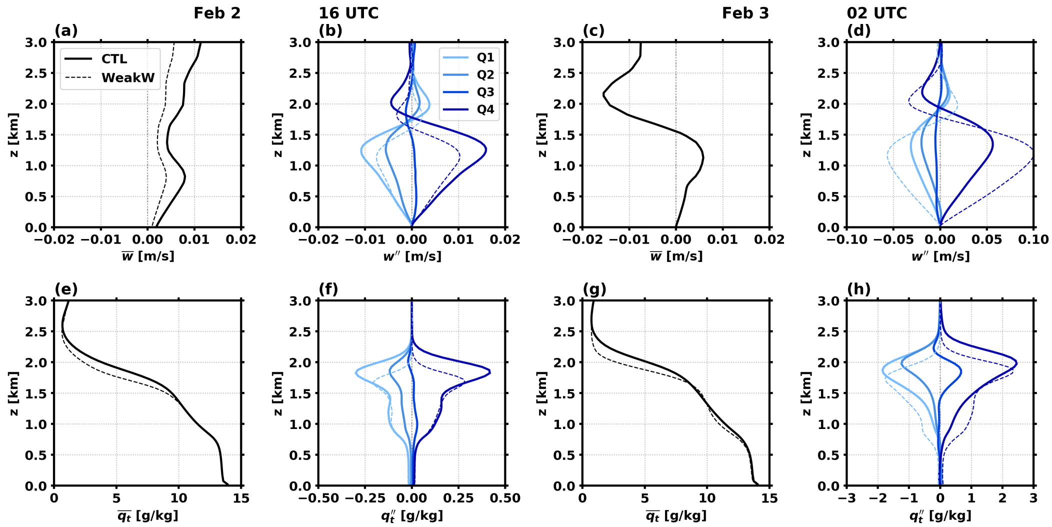

Figure 3. Vertical profiles of various variables at 16 UTC on February 2 (two left columns) and 2 UTC on February 3 (two right columns) of both CTL (solid) and WeakW (dash): (a,c) domain-mean vertical velocity ($\overline{w}$); (b,d) mesoscale perturbations of vertical velocity binned by TWP quartiles (w''); (e,g) domain-mean total water mixing ratio ($\overline{q_t}$); and (f,h) mesoscale perturbations of total water (q_t''), binned by TWP quartiles. For the binned profiles, only Q1 and Q4 from WeakW are shown.

asymmetrical; the moist areas become moister while the dry areas become drier (Fig. 2e). The variance of TWP normalized by the mean can be used as a proxy for the organization (Fig. 2f). The coarse-grained normalized TWP variance (green) increases several hours after the full 100 m resolution normalized variance (black), evidence that the moist patches are initially smaller than 16 km and later grow during the transition. The domain-mean optical depth (OPD) also increases, except for a dip around 21 UTC (Fig. 2g), when the small isolated sugar clouds disappear while the larger cloud clusters have yet to aggregate and grow (Fig. 1e). After 20 UTC, both the normalized TWP variance and the OPD increase rapidly as the organization strengthens.

Figure 3 shows the vertical profiles at two different times, during and after the transition. At both times, regardless of $\overline{w}$, the binned mesoscale vertical velocity perturbations (w'') are positive in the cloud and subcloud layers and negative in the inversion layer of the moistest quartile (Q4). In the drier quartiles (Q1-Q2), the signs of w'' are opposite. The moist quartiles also have positive mesoscale total water perturbations (q_t''). Mass continuity requires that in the moist and cloudy regions, where w'' is positive (negative) in the subcloud (inversion) layer, there is a local convergence (divergence) below (aloft), consistent with the findings in Bretherton and Blossey (2017). The following section will show that this local circulation is key for redistributing the total water, leading to mesoscale organization.

4 The Mechanism of Transition

This section analyzes the budget of mesoscale total water perturbations q_t'' in the four TWP quartiles to determine a mechanism responsible for the transition. Based on Equation 12 of Bretherton and Blossey (2017) and the derivation in Section 3 of the SI, the budget of q_t'' at each level can be written as:

$$\frac{\partial q_t''}{\partial t} = A + B + C + S_q'' \quad . \tag{2}$$

Each term on the right hand side of Equation (2) is described as follows: The first term is the advection of mesoscale variability due to trajectory-relative large-scale wind ($\overline{\boldsymbol{v}}$) and mesoscale perturbations of the wind velocity ($\boldsymbol{v}''$):

$$A = -(\overline{\boldsymbol{v}} + \boldsymbol{v}'') \cdot \nabla q_t'' \quad . \tag{3}$$

Let [ ] denote coarse-graining of the cumulus-scale field inside the brackets to a mesoscale region of 16×16 km^2, and let ρ denote the reference density profile. The second term represents the vertical and horizontal gradients of the cumulus-scale q_t flux coarse-grained to 16×16 km^2:

$$B = B_v + B_h = -\frac{1}{\rho}\frac{\partial}{\partial z}[\rho w''' q_t'''] - \nabla_h \cdot [\boldsymbol{v}''' q_t'''] \quad . \tag{4}$$

Eq. (4) was derived with the anelastic approximation used in SAM. The third term is the mesoscale vertical advection of large-scale q_t:

$$C = -w'' \frac{\partial \overline{q_t}}{\partial z} \quad . \tag{5}$$

Finally, the fourth term (Fig. 4d) is the source term of q_t'' which represents the divergence of precipitation mass flux (F_p):

$$S_q'' = (-\frac{1}{\rho}\frac{\partial F_p}{\partial z})'' \quad . \tag{6}$$

Figure 4(a-d) shows vertical profiles of A, B_v, B_h, and C binned by TWP quartiles at the end of CTL, and the vertically integrated values between 0 and 3 km (denoted by $\langle \quad \rangle$). (The S_q'' profiles and their vertically integrated values are much smaller

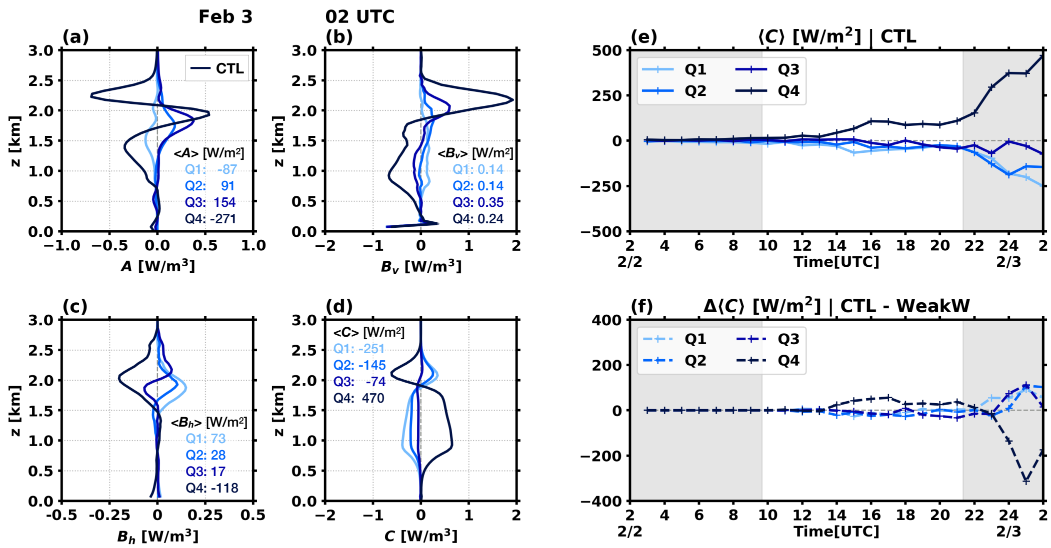

Figure 4. Vertical profiles of: (a) large-scale and mesoscale advection of q_t'' (A); (b) vertical gradient of the cumulus-scale vertical q_t flux (B_v); (c) horizontal gradient of the cumulus-scale horizontal q_t flux (B_h); and (d) mesoscale vertical advection of the large-scale q_t (C), at 2 UTC on February 3 from CTL, all coarse-grained to 16×16 km^2 and binned by TWP. The vertically integrated values between 0 and 3 km are also shown, denoted by $\langle \quad \rangle$. (g) Hourly time series of $\langle C \rangle$ binned by TWP quartiles from CTL. (h) The change in $\langle C \rangle$ time series between CTL and WeakW.

and hence negligible, as shown in Figure S6.) A positive quantity means the respective term is responsible for moistening the region.

In Q4, A is small and tends to dry out the boundary layer. Although B_v is large, $\langle B_v \rangle$ is negligible in all quartiles. This is expected because the vertical cumulus-scale flux transfers total water vertically from the cloud layer to the inversion layer but not horizontally. When coarse-grained within 16×16 km^2 regions, B_h is small, but $\langle B_h \rangle$ is non-negligible and results in drying in Q4, albeit secondary to $\langle A \rangle$. The magnitude of C is larger than that of A and B_h, and $\langle C \rangle$ is the only term that moistens the cloud layer in Q4, in which flower clouds aggregate. Because $\frac{\partial \overline{q_t}}{\partial z}$ is always negative (Fig. 3e,g), the sign of C always follows the sign of w''. Due to mass continuity, a positive C in the cloud layer of Q4 is associated with a horizontal total water convergence below the cloud plumes, and divergence in the inversion. A positive $\langle C \rangle$ indicates a net total water convergence in the lower troposphere of the moistest quartile.

To demonstrate that $\langle C \rangle$ drives moistening in Q4 and drying in Q1 through Q3, Figure 4(e) shows the hourly time series of $\langle C \rangle$ binned by TWP quartiles from CTL. This provides the evidence that the net convergence and divergence of total water due to mesoscale circulation renders the moist and cloudy patches moister, and the dry and cloud-free patches drier.

5 The Role of Large-Scale Vertical Motion

To examine the role of large-scale vertical velocity for the sugar-to-flower transition, an additional simulation is performed and analyzed. Simulation WeakW has a 50 % weaker $\overline{w}$ during the period of strong upward motion, i.e., 10 UTC and 20 UTC (Fig. 2c). It produces a shallower cloud layer and lower TWP than CTL. Movie S3 shows the cloud field evolution in WeakW. Simulation CTL exhibits a more rapid transition from the sugar to the flower cloud state (Fig. S7). It has greater normalized TWP variance and optical depth, especially in Q4 where flowers aggregate (Fig. 2f,i).

Although mesoscale organization forms more rapidly in CTL compared to WeakW, the same mechanisms take place in both simulations; moist areas become moister and dry areas become drier. Figure 3b,f shows that with stronger upward motion, the w'' and q_t'' profiles of CTL during the transition period have the same structure as those in WeakW, except with larger magnitudes. After 23 UTC, when the organization in WeakW catches

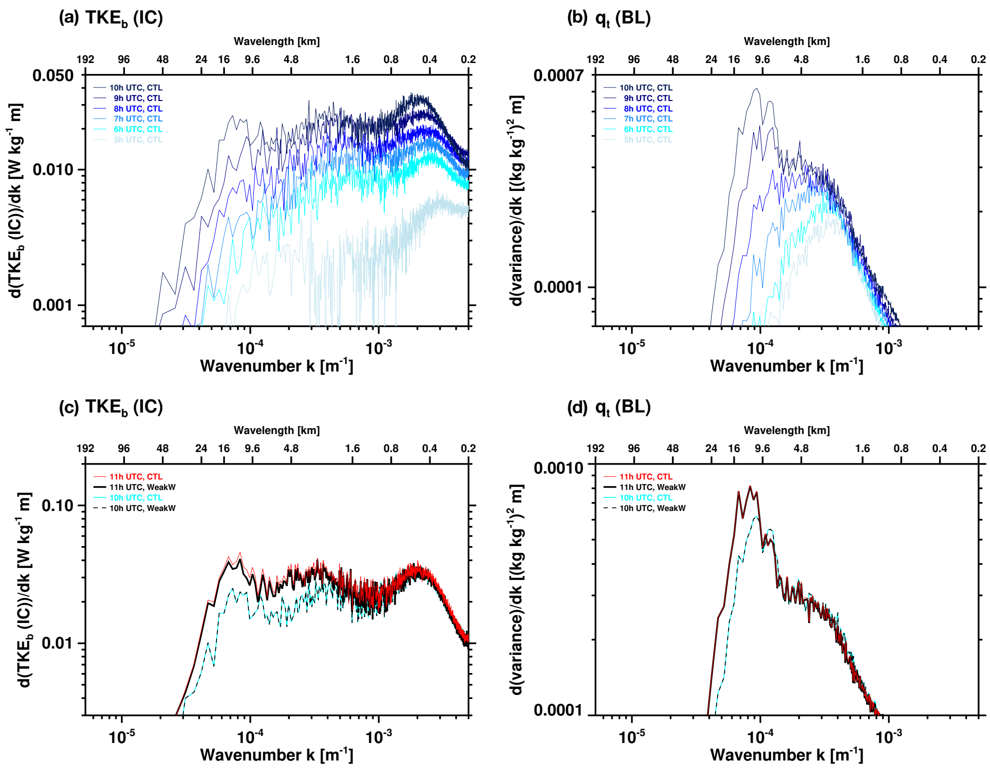

Figure 5. Spectra of (a) buoyant turbulence kinetic energy production in the cloud layer (TKE$_b$(IC)), expressed in units of W kg^{-1} of boundary-layer mass, and of (b) total water mixing ratio in the boundary layer (q$_t$(BL)), from CTL, plotted hourly from 5 UTC to 10 UTC on February 2. Spectra of (c) TKE$_b$(IC) and (d) q_t(BL), from CTL and WeakW at 10 UTC and 11 UTC on February 2.

up with CTL, w'' becomes stronger in WeakW compared to CTL (Fig. 3h). This is consistent with the change in $\langle C \rangle$, which is greater in Q4 of CTL compared to WeakW between 10 UTC and 23 UTC (Fig. 4f), and smaller thereafter. In other words, the stronger upward motion assists the aggregation of total water on the mesoscale, accelerating organization.

Figure 5 shows spectra of buoyant turbulence kinetic energy (TKE) production in the cloud layer (TKE$_b$(IC)) and of boundary-layer total water (q_t(BL)). Circulation on the mesoscale and aggregation of moisture emerge in the form of peaks between 9.6 and 16 km that are clearly discernible by 10 UTC (Fig. 5a,b). Up to 10 UTC, CTL and WeakW have the same $\overline{w}$, hence their TKE production spectra are identical, but at 11 UTC, CTL exhibits a strengthening of cloud-level TKE production on the mesoscale (Fig. 5c). In the sub-cloud layer, TKE production exhibits a much weaker response (Fig. S9b). This disproportionate strengthening of cloud-level mesoscale TKE production relative to other scales, due to the more positive $\overline{w}$ in CTL compared to WeakW, increases and persists over the period during which $\overline{w}$ differs between the simulations (Fig. S10). No discernible difference exists in the spectra of total water at 11 UTC (Fig. 5d), and only after several hours does a stronger mesoscale peak emerge in CTL compared to WeakW (Fig. S11). It is hence the strengthening of cloud-level mesoscale TKE production that strengthens aggregation of moisture on the mesoscale and accelerates the sugar-to-flower transition in response to a more positive $\overline{w}$.

6 Conclusions

The ATOMIC and EUREC^{4}A field campaign took place in the Atlantic Ocean east of Barbados in January–February 2020, with a goal to better understand the relationship between shallow cumuli and large-scale meteorological and oceanic conditions. On February 2–3, a transition of trade cumulus organization from sugar to flowers was observed. This study shows that a Lagrangian LES following a boundary-layer airmass trajectory can reproduce the transition. During the sugar-to-flowers transition, the clouds become organized, and the cloud layer deepens and moistens.

Although the large-scale vertical wind helps deepen the cloud layer, the mesoscale wind drives the sugar-to-flowers transition. The mesoscale circulation, driven by a local ascending (descending) air inside (above) the shallow cumulus plumes, leads to a net moisture convergence in the moist patches, in which the clouds aggregate. This renders the moist patches moister and dry patches drier.

It is shown that large-scale vertical velocity regulates the sugar-to-flower transition by modulating cloud-layer buoyant TKE production at the mesoscale, and the mesoscale circulation by which moisture aggregates. In the considered case, stronger large-scale upward motion accelerates the sugar-to-flower transition by strengthening cloud-layer mesoscale TKE production. Given the broad interest in the vertical structure of subsidence engendered by ATOMIC and EUREC^{4}A, a follow-on study examining how the structure of the large-scale vertical velocity impacts the mesoscale organization is warranted.

Acknowledgments

This study was supported by NOAA's Climate Program Office, Climate Variability and Predictability Program (GC19-303). This is PMEL contribution number: 5239. The authors thank scientists, technicians, pilots, crew members, and everybody who made the ATOMIC and EUREC^{4}A field campaign possible. We thank Marat Khairoutdinov, Stony Brook University, for providing the System for Atmospheric Modeling (SAM). We acknowledge the NOAA Research and Development High Performance Computing Program for providing computing and storage resources that have contributed to the research results reported within this paper. ERA5 data were generated using Copernicus Climate Change Service Information. Neither the European Commission or ECMWF is responsible for any use that may be made of the Copernicus information or data in this publication. Simulation outputs from this study are available at `https://csl.noaa.gov/groups/csl9/datasets/data/cloud_phys/2021-Narenpitak-etal/`.

References

Blossey, P. N., Bretherton, C. S., Zhang, M., Cheng, A., Endo, S., Heus, T., ... Xu, K. M. (2013). Marine low cloud sensitivity to an idealized climate change: The CGILS les intercomparison. *Journal of Advances in Modeling Earth Systems*, *5*(2), 234–258. doi: 10.1002/jame.20025

Bony, S., & Dufresne, J. L. (2005). Marine boundary layer clouds at the heart of tropical cloud feedback uncertainties in climate models. *Geophysical Research Letters*, *32*(20), 1–4. doi: 10.1029/2005GL023851

Bony, S., Schulz, H., Vial, J., & Stevens, B. (2020). Sugar, Gravel, Fish, and Flowers: Dependence of Mesoscale Patterns of Trade-Wind Clouds on Environmental Conditions. *Geophysical Research Letters*, *47*(7), 1–9. doi: 10.1029/2019gl085988

Boucher, O., Randall, D., Artaxo, P., Bretherton, C., Feingold, G., Forster, P., ... Zhang, X. Y. (2013). Clouds and aerosols. In *Climate change 2013 the physical science basis: Working group i contribution to the fifth assessment report of the intergovernmental panel on climate change.* doi: 10.1017/CBO9781107415324.016

Bretherton, C. S., & Blossey, P. N. (2017). Understanding Mesoscale Aggregation of Shallow Cumulus Convection Using Large-Eddy Simulation.

Journal of Advances in Modeling Earth Systems, *9*(8), 2798–2821. doi: 10.1002/2017MS000981

Bretherton, C. S., Blossey, P. N., & Jones, C. R. (2013). Mechanisms of marine low cloud sensitivity to idealized climate perturbations: A single-LES exploration extending the CGILS cases. *Journal of Advances in Modeling Earth Systems*, *5*(2), 316–337. doi: 10.1002/jame.20019

Feingold, G., Walko, R. L., Stevens, B., & Cotton, W. R. (1998). Simulations of marine stratocumulus using a new microphysical parameterization scheme. *Atmospheric Research*, *47–48*, 505–528. doi: 10.1016/S0169-8095(98)00058-1

Hersbach, H., Bell, B., Berrisford, P., Hirahara, S., Horányi, A., Muñoz-Sabater, J., ... Thépaut, J.-N. (2020). The era5 global reanalysis. *Quarterly Journal of the Royal Meteorological Society*, *146*(730), 1999-2049. Retrieved from `https://rmets.onlinelibrary.wiley.com/doi/abs/10.1002/qj.3803` doi: https://doi.org/10.1002/qj.3803

Khairoutdinov, M. F., & Randall, D. A. (2003). Cloud Resolving Modeling of the ARM Summer 1997 IOP: Model Formulation, Results, Uncertainties, and Sensitivities. *Journal of the Atmospheric Sciences*, *60*(4), 607–625. doi: 10.1175/1520-0469(2003)060⟨0607:CRMOTA⟩2.0.CO;2

Mieslinger, T., Horváth, Á., Buehler, S. A., & Sakradzija, M. (2019). The Dependence of Shallow Cumulus Macrophysical Properties on Large-Scale Meteorology as Observed in ASTER Imagery. *Journal of Geophysical Research: Atmospheres*, *124*(21), 11477–11505. doi: 10.1029/2019JD030768

Mlawer, E. J., Taubman, S. J., Brown, P. D., Iacono, M. J., & Clough, S. A. (1997). Radiative transfer for inhomogeneous atmospheres: RRTM, a validated correlated-k model for the longwave. *Journal of Geophysical Research: Atmospheres*, *102*(D14), 16663-16682. doi: 10.1029/97JD00237

Narenpitak, P., & Bretherton, C. S. (2019). Understanding Negative Subtropical Shallow Cumulus Cloud Feedbacks in a Near-Global Aquaplanet Model Using Limited Area Cloud-Resolving Simulations. *Journal of Advances in Modeling Earth Systems*, *11*(6), 1600–1626. doi: 10.1029/2018MS001572

Pincus, R., Fairall, C. W., Bailey, A., Chen, H., Chuang, P. Y., de Boer, G., ... Zuidema, P. (2021). Observations from the noaa p-3 aircraft during atomic. *Earth System Science Data Discussions*, *2021*, 1–25. Retrieved from https://essd.copernicus.org/preprints/essd-2021-11/ doi: 10.5194/essd-2021-11

Quinn, P. K., Thompson, E., Coffman, D. J., Baidar, S., Bariteau, L., Bates, T. S., … Zuidema, P. (2020). Measurements from the *RV Ronald H. Brown* and related platforms as part of the atlantic tradewind ocean-atmosphere mesoscale interaction campaign (atomic). *Earth System Science Data Discussions*, *2020*, 1–41. Retrieved from https://essd.copernicus.org/preprints/essd-2020-331/ doi: 10.5194/essd-2020-331

Rasp, S., Schulz, H., Bony, S., & Stevens, B. (2020). Combining crowd-sourcing and deep learning to explore the meso-scale organization of shallow convection. *Bulletin of the American Meteorological Society*, *101*(11), E1980–E1995. doi: 10.1175/BAMS-D-19-0324.1

Rolph, G., Stein, A., & Stunder, B. (2017). Real-time environmental applications and display system: Ready. *Environmental Modelling and Software*, *95*, 210-228. doi: https://doi.org/10.1016/j.envsoft.2017.06.025

Siebesma, a. P., Bretherton, C. S., Brown, A., Chlond, A., Cuxart, J., Duynkerke, P. G., … Stevens, D. E. (2003). A Large Eddy Simulation Intercomparison Study of Shallow Cumulus Convection. *Journal of the Atmospheric Sciences*, *60*(10), 1201–1219. doi: 10.1175/1520-0469(2003)60⟨1201:ALESIS⟩2.0.CO;2

Stein, A. F., Draxler, R. R., Rolph, G. D., Stunder, B. J. B., Cohen, M. D., & Ngan, F. (2015). Noaa's hysplit atmospheric transport and dispersion modeling system. *Bulletin of the American Meteorological Society*, *96*(12), 2059 - 2077. doi: 10.1175/BAMS-D-14-00110.1

Stevens, B., Bony, S., Brogniez, H., Hentgen, L., Hohenegger, C., Kiemle, C., … Zuidema, P. (2020). Sugar, gravel, fish and flowers: Mesoscale cloud patterns in the trade winds. *Quarterly Journal of the Royal Meteorological Society*, *146*(726), 141–152. doi: 10.1002/qj.3662

Stevens, B., Bony, S., Farrell, D., Ament, F., Blyth, A., Fairall, C., … Zöger, M. (2021). Eurec^{4}a. *Earth System Science Data Discussions*, *2021*, 1–78. Retrieved from https://essd.copernicus.org/preprints/essd-2021-18/ doi: 10.5194/essd-2021-18

Zelinka, M. D., Zhou, C., & Klein, S. A. (2016). Insights from a refined decomposition of cloud feedbacks. *Geophysical Research Letters*, *43*, 9259–9269. doi: 10

.1002/2016GL069917

Zhang, M., Bretherton, C. S., Blossey, P. N., Austin, P. H., Bacmeister, J. T., Bony, S., ... Zhao, M. (2013). CGILS: Results from the first phase of an international project to understand the physical mechanisms of low cloud feedbacks in single column models. *Journal of Advances in Modeling Earth Systems*, *5*(4), 826–842. doi: 10.1002/2013MS000246

Zuidema, P., Torri, G., Muller, C., & Chandra, A. (2017). A Survey of Precipitation-Induced Atmospheric Cold Pools over Oceans and Their Interactions with the Larger-Scale Environment. *Surveys in Geophysics*, *38*(6), 1283–1305. doi: 10.1007/s10712-017-9447-x